July, 2013

Airborne Dual-Polarization Observations of the Sea-Surface NRCS at C-band in High Winds

Joseph W Sapp, *University of Massachusetts - Amherst*
Stephen J Frasier, *University of Massachusetts - Amherst*
Jason Dvorsky, *University of Massachusetts - Amherst*
Paul S Chang
Zorana Jelenak

Airborne Dual-Polarization Observations of the Sea-Surface NRCS at C-band in High Winds

Joseph W. Sapp, *Student Member, IEEE,* Stephen J. Frasier, *Senior Member, IEEE,* Jason Dvorsky, *Student Member, IEEE,* Paul S. Chang, *Member, IEEE,* and Zorana Jelenak, *Member, IEEE*

***Abstract*—Airborne dual-polarization observations of sea-surface normalized radar cross-section (NRCS) were conducted over the North Atlantic during Jan–Feb 2011. Observations were made using the University of Massachusetts' Imaging Wind and Rain Airborne Profiler (IWRAP) radar system installed on the National Oceanic and Atmospheric Administration's (NOAA) WP-3D research aircraft during several winter storm events to determine the high-wind response of the sea-surface NRCS for both horizontal and vertical polarizations. During the flights, the aircraft performed several constant-roll circle maneuvers to allow collection of NRCS over a range of incidence angles. We find consistency with prior reports in the polarization ratio observed at moderate incidence angles at the winds encountered. For larger incidence angles, we observe a measurable decrease in polarization ratio with increasing wind speed.**

***Index Terms*—C-band, ocean winds, polarization ratio, scatterometry.**

I. Introduction

SATELLITE-BORNE observations of sea surface backscatter are routinely used to estimate winds. Currently, the Advanced Scatterometer (ASCAT) aboard the European METOP-1 satellite measures sea surface winds using C-band vertical polarization. The Canadian RADARSAT-2 SAR instrument also operates at C-band measuring both V- and H-polarizations. Though primarily designed for high-resolution imaging, there have been a number of recent efforts to infer wind speed and direction from C-band RADARSAT SAR imagery [1], [2], most recently on the potential utility of cross-polarized measurements [3], [4]. Use of C-band is also being explored in designs for a future US scatterometer to replace the now-defunct Ku-band QuikSCAT instrument. As C-band is less prone to attenuation in precipitation, it is more robust in the presence of rain than is Ku-band. However, since Ku-band offers finer spatial resolution for a given antenna size, future scatterometry missions are expected to incorporate both frequencies.

During January and February 2011 a series of flight experiments were conducted over the North Atlantic in extratropical storms to obtain observations of the sea surface under strong wind forcing. In particular, it was desired to extend rain-free, high-wind normalized radar cross-section (NRCS), or σ^0, observations at VV- and HH-polarizations to incidence angles near and beyond 60°. In this letter we briefly describe the radar instrumentation, flight experiments, and the results of several circle flights, from which the incidence angle and azimuthal dependence at one C-band frequency were investigated.

Manuscript received April 2, 2012; revised August 22, 2012; accepted September 17, 2012. This work was supported by NASA under JPL contract 1424244 to the University of Massachusetts and by the NOAA Ocean Winds program.

J. W. Sapp, S. J. Frasier, and J. Dvorsky are with the Microwave Remote Sensing Laboratory, University of Massachusetts, Amherst, MA 01003 USA.

P. S. Chang and Z. Jelenak are with the NOAA/NESDIS Center for Satellite Applications Research, Camp Springs, MD 20746 USA.

Color versions of one or more of the figures in this paper are available online at http://ieeexplore.ieee.org.

Digital Object Identifier 10.1109/LGRS.2012.2220118

TABLE I
C-band Radar Parameters

Parameter	Chan. 1	Chan. 2
Frequency (GHz)	5.025	5.2
Nom. Incidence Angle	46.4°(H), 46.7°(V)	34.0°(H), 36.0°(V)
Pulse Rate (kHz)	15	15
Pulse width (μs)	10 (chirp)	0.8 (pulse)
Antenna Gain (dB)	21.4(H), 24.9(V)	23.9(H), 25.1(V)
Azimuthal Beamwidth	10.1°(H), 9.9°(V)	13.5°(H), 12.2°(V)
Scan Rate (rpm)	60	60

II. Experiment Description

The Imaging Wind and Rain Airborne Profiler (IWRAP), initially described in [5], is a dual-frequency conically-scanning Doppler radar developed by the Microwave Remote Sensing Laboratory at the University of Massachusetts (MIRSL) that is routinely installed on the National Oceanic and Atmospheric Administration's (NOAA) WP-3D research aircraft. IWRAP is primarily designed to study the signature of the ocean surface under wind forcing. Two radars (one C-band and one Ku-band) scan at two incidence angles each, typically between 20° and 50°. Each radar is capable of implementing up to four simultaneous beams, however, two simultaneous beams per radar is the normal mode of operation. Both VV- and HH-polarizations are available and are selected based upon mission requirements. The radar beam widths vary depending upon the selected incidence angle owing to properties of the frequency-scanning antenna, but are typically in the neighborhood of 10°. For the Winter 2011 mission, IWRAP was configured to measure VV- and HH-polarizations by toggling rapidly between them during each azimuthal scan. Table I summarizes the C-band radar parameters during data collection.

The IWRAP geophysical model function was developed for several fixed incidence angles between 30° and 50° at VV- and HH-polarizations [6]. The goal of the Winter 2011 experiment was to obtain rain-free sea-surface NRCS observations over a

TABLE II
SUMMARY OF THE WINTER 2011 FLIGHT EXPERIMENT

Date	Times (UTC)	Circles Executed	Wind Speeds ($\mathrm{m\,s^{-1}}$)
20110123	1600–2000	3	19–24
20110124	1600–2000	8	21–27
20110130	1700–2100	5	18–24
20110201	1600–1900	6	25–36
20110207	1600–1900	6	23–31

continuous range of incidence angles between 20° and 60° at both VV- and HH-polarizations. The most expedient means to accomplish this is to fly the aircraft in a circular pattern at a constant roll angle. In this way, the conically scanning beam impinging on the sea surface traces out an ellipse with incidence angles varying with the azimuthal scan angle. The range of incidence angles encountered is given by the nominal (level flight) incidence angle plus or minus the roll angle. Since the incidence angle varies with the azimuthal angle, and since the NRCS also varies with azimuth angle (relative to the wind direction), a circle pattern ensures that all incidence angles are observed from all directions.

Surface wind speeds were measured simultaneously with the Stepped Frequency Microwave Radiometer (SFMR) [7] operated by the NOAA Aircraft Operations Center aboard the WP-3D aircraft. Since the SFMR is a nadir-looking instrument, we use the mean wind speed from the retrievals before and after a roll as the wind speed during a roll. Several missions were flown out of Halifax, NS during January–February 2011; Table II contains a summary of the Winter 2011 flight experiment.

III. Data Processing Methodology

During the Winter 2011 experiment, the IWRAP radar alternated between polarizations by transmitting a sequence of 126 pulses in each polarization. Raw I- and Q-channel samples were collected and recorded. In post-processing, some of these data were subject to pulse compression; Doppler spectrum moments were then accumulated over each 126-pulse block using pulse-pair methods [8]. The resulting profiles of backscatter and Doppler velocity are available at a rate of approximately 60 Hz per polarization. Given the azimuthal scan rate of the antenna, there are approximately 60 radials in each 360° scan of the antenna (one per second). The resulting profiles are then merged with navigation parameters (pitch, roll, drift, etc. available at a 40 Hz rate) and simultaneous surface wind speed estimates from the SFMR (available at a 1 Hz rate).

Once merged, the data are sorted by incidence and azimuth angle. The incidence angle is derived from navigation parameters and antenna azimuth information using methods described in [9]. This is checked for consistency against a separate radar estimate from the arc-cosine of the ratio of the slant range to the surface echo and the aircraft altitude. Similarly, antenna azimuth is verified by a check against the observed Doppler shift from the sea surface after appropriate transformations for pitch, roll, and drift.

Although a range of incidence angles may be observed during the circle patterns, there is a small source of error due to polarization mixing. That is, given the finite roll angle, the polarization incident upon the sea surface is only truly the polarization transmitted and received at the extreme incidence angles (when the antenna is scanning to the side of the aircraft). A small correction is applied given the aircraft attitude and antenna azimuth to account for this mixing.

NRCS is estimated from the echo using a pulse-limited surface area given an estimate of the transmitted power provided by an internal calibration loop. Although 126 points are averaged to obtain an NRCS estimate, the number of independent samples is approximately 7–8. Any profile with a measurable precipitation echo in the atmosphere between the aircraft and surface is considered to be contaminated by rain and is discarded.

Upon averaging many estimates, residual biases are inevitably observed in the data due to uncompensated system losses (e.g. feed lines, wet radome from previous flight through rain, etc.). A final adjustment is applied to the NRCS observed during a particular flight. For each circle during the flight and at each polarization, the difference between the observed mean NRCS and a known geophysical model function (GMF) at a known incidence angle and wind speed is computed. The mean adjustment is then applied to all circles in the flight. The wind speed used for each calculation is the mean wind speed observed within its wind speed group; it is obtained from the SFMR and is indicative of the neutral stability wind speed at 10 m height. The model function used is the IWRAP model; valid for VV- and HH-polarizations but only at specific incidence angles [6]. The incidence angle used is the largest incidence angle available for the GMF at the corresponding polarization.

IV. Results

Fig. 1 shows a summary of data collected by the C-band VV-polarization radar during one of the circle patterns flown on January 24, 2011. The top panel shows NRCS as a function of the computed incidence angle (but for all aircraft headings, hence all wind directions). The individual NRCS samples collected during the circle pattern are shown as gray dots. The mean, shown as a solid line, indicates the mean NRCS—the A_0 term in the typical scatterometer directional signature, i.e.,

$$\sigma^0 = A_0 + A_1 \cos\chi + A_2 \cos 2\chi \qquad (1)$$

where χ is the wind-relative look direction. This and subsequent mean NRCS lines don't necessarily match up with the IWRAP GMF at 50°; this is a result of applying one final adjustment per polarization to all NRCS from this flight. When the aircraft heading is added to the track-relative azimuth, one obtains the compass direction. The bottom panel shows the NRCS versus compass direction, revealing the scatterometer directional signature of (1). The mean NRCS over compass direction for approximately 50° incidence at $22.5\,\mathrm{m\,s^{-1}}$ is shown as a solid line. The CMOD5.N [10] and IWRAP VV-polarization GMFs are also shown. Since the IWRAP GMF is only defined for a few incidence angles, its values are shown as unconnected filled circles.

Fig. 2 shows a summary of mean NRCS over all observation directions, or the A_0 term in (1), as a function of incidence

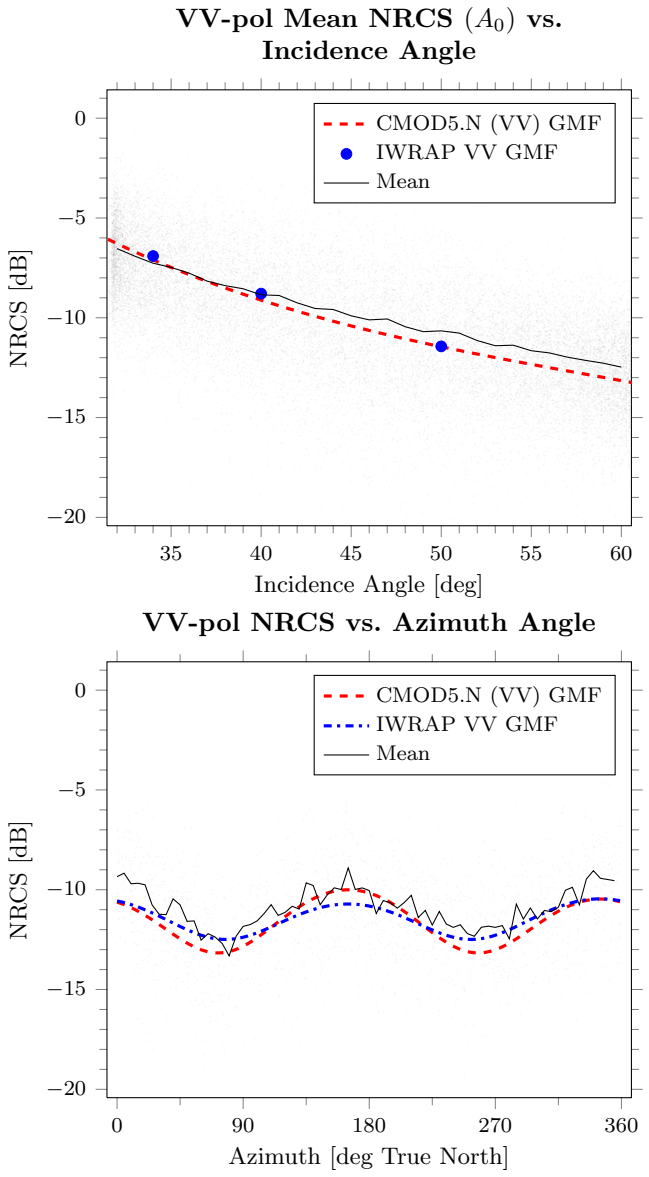

Fig. 1. Summary from a circle pattern flown on January 24, 2011 for C-band VV-polarization. The wind speed was $22.5\,\mathrm{m\,s^{-1}}$. The CMOD5.N and the IWRAP VV-polarization GMF are also shown at the wind speeds for which they are defined. (Top) VV-polarized NRCS (A_0) versus incidence angle for all azimuthal directions. Each NRCS sample collected is shown as a gray dot. The mean NRCS is shown as a solid line. CMOD5.N is shown as a dashed line and values from the IWRAP GMF are shown as filled circles at the incidence angles for which it is valid. (Bottom) VV-polarized NRCS versus azimuth. Each NRCS sample is shown as a gray dot. All samples between $48°$ and $52°$ incidence are averaged every $5°$ in azimuth and are connected with a solid line. CMOD5.N is shown as a dashed line and the IWRAP GMF at $50°$ incidence is shown as a dash-dotted line.

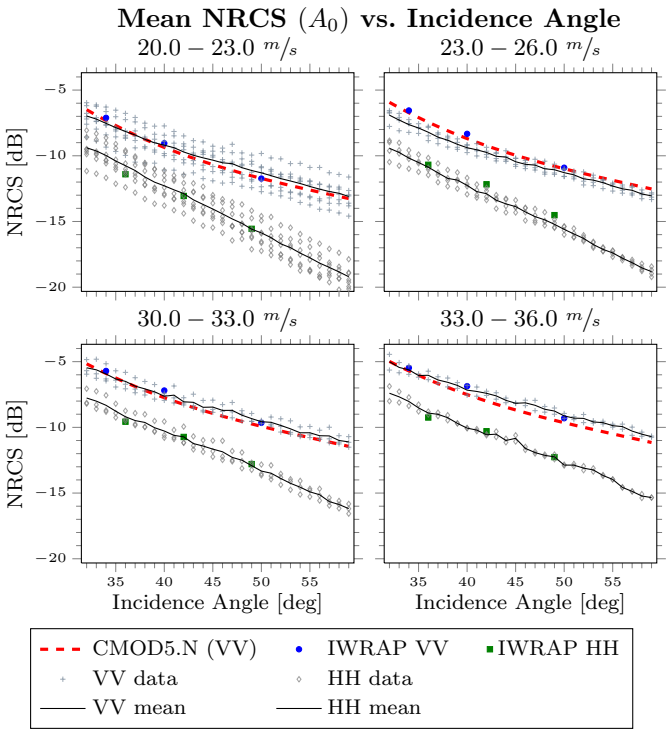

Fig. 2. Mean NRCS (A_0) versus incidence angle for circle patterns flown on all dates in the Winter 2011 experiment grouped by wind speed. The model functions shown are computed with the mean wind speed in each wind speed range. Mean NRCS samples at each incidence angle from each circle are shown as gray plus symbols (VV-pol) and gray diamond symbols (HH-pol). The uncertainties of these means are no greater than $0.4\,\mathrm{dB}$. The mean of all samples within a wind speed bin is shown as a solid line. CMOD5.N is shown as a dashed line. The IWRAP VV-pol and HH-pol GMFs are shown as filled circles and squares, respectively, at the incidence angles for which they are valid.

angle for all dates in the Winter 2011 experiment at C-band at both VV- and HH-polarizations. For a given wind speed range, each data point is the A_0 value for one circle pattern at one polarization at one incidence angle, $\pm 0.5°$. The mean of these points are shown as a solid line. In addition, shown are the A_0 values for the IWRAP model function at the incidence angles for which it is defined and the CMOD5.N model function averaged over all azimuth angles. The data in the lowest wind speed group show more scatter than the higher wind speeds. This is influenced by the increased uncertainty in wind speed retrieval from the SFMR below about $22\,\mathrm{m\,s^{-1}}$. The VV-polarization data compare well with both the CMOD5.N and IWRAP A_0 at all incidence angles shown and over all wind speeds sampled. The IWRAP HH model function compares well with the HH-polarized data for the larger two incidence angles shown; however, the IWRAP HH GMF differs from the observations at the smallest incidence angle shown. The trend in NRCS over incidence angle observed during the Winter 2011 experiment is consistent with that of CMOD5.N.

Fig. 3 shows the polarization ratio as a function of incidence angle for all dates in the Winter 2011 experiment at C-band. For a given wind speed range, the gray circles are the ratio VV/HH of the mean A_0 at each incidence angle for one complete circle. The wind-speed-independent polarization ratio models from [3], [4], [11] are also shown. In the lowest two wind speed groups, the ratios observed in the Winter 2011 data match reasonably well with the ratio from [3] and with Model 1 from [4] for incidence angles greater than $40°$. As the wind speed increases, the incidence angle dependence on polarization ratio decreases and cannot be represented by any of the models shown. At incidence angles below $40°$, the ratio begins to flatten out slightly. We expect that the ratio should continue to trend towards unity as the incidence angle

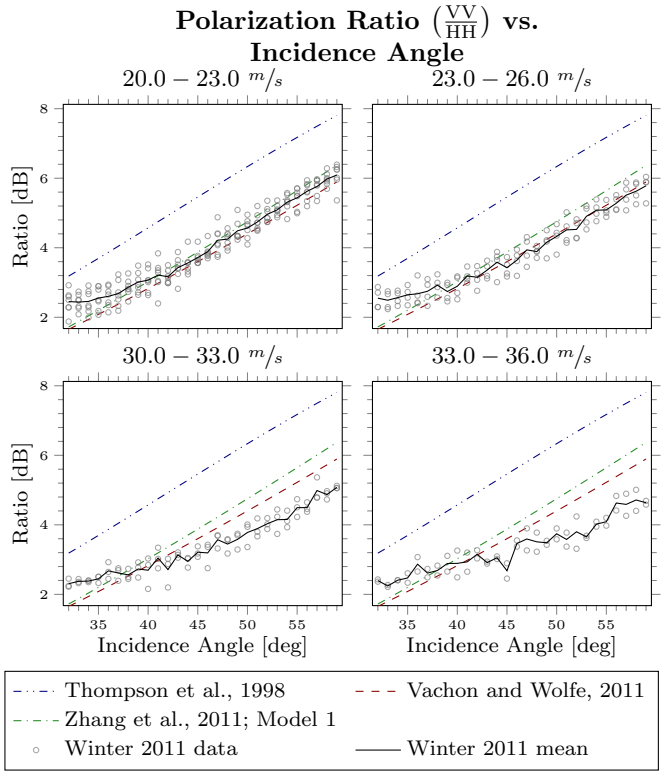

Fig. 3. Polarization ratio VV/HH versus incidence angle grouped by wind speed. Ratios of the mean NRCS samples at each incidence angle from each circle are shown as gray circles. The mean of these is shown as a solid line. Polarization ratio models from [3], [4], [11] are also shown for reference.

TABLE III
COEFFICIENTS FOR THE FIT OF THE MEAN VV-POLARIZED NRCS AS A FUNCTION OF WIND-RELATIVE AZIMUTH ANGLE TO $A + B\cos\,\chi + C\cos\,2\chi$ IN LINEAR UNITS

Wind Speed Group ($\mathrm{m\,s^{-1}}$)	A	B	C
20.0–23.0	1.0168	$1.8716 \cdot 10^{-3}$	$6.2065 \cdot 10^{-3}$
23.0–26.0	1.0171	$1.3911 \cdot 10^{-3}$	$5.6421 \cdot 10^{-3}$
30.0–33.0	1.0254	$1.4188 \cdot 10^{-4}$	$4.6547 \cdot 10^{-3}$
33.0–36.0	1.0285	$1.8897 \cdot 10^{-4}$	$4.6014 \cdot 10^{-3}$

approaches nadir. This divergence from the models may be anticipated; we note both the ratios from [3] and Model 1 from [4] reach unity around 20° incidence.

Assuming a constant wind field over the area sampled during the circle pattern, the NRCS directional signature can be investigated. Fig. 4 shows NRCS versus wind-relative azimuth angle (χ) at 50° incidence for the same wind speed bins and in the same manner as Fig. 2. The scatterometer directional signature of (1) is visible in all plots. As expected, with increasing wind speed the amplitude decreases, and wind direction is more difficult to unambiguously determine. In addition, shown are the CMOD5.N and IWRAP GMFs at 50° incidence.

TABLE IV
COEFFICIENTS FOR THE FIT OF THE MEAN HH-POLARIZED NRCS AS A FUNCTION OF WIND-RELATIVE AZIMUTH ANGLE TO $A + B\cos\,\chi + C\cos\,2\chi$ IN LINEAR UNITS

Wind Speed Group ($\mathrm{m\,s^{-1}}$)	A	B	C
20.0–23.0	1.0059	$1.4591 \cdot 10^{-3}$	$2.0956 \cdot 10^{-3}$
23.0–26.0	1.0063	$1.1929 \cdot 10^{-3}$	$2.1497 \cdot 10^{-3}$
30.0–33.0	1.0109	$2.0066 \cdot 10^{-3}$	$1.9351 \cdot 10^{-3}$
33.0–36.0	1.0126	$1.5882 \cdot 10^{-3}$	$1.2505 \cdot 10^{-3}$

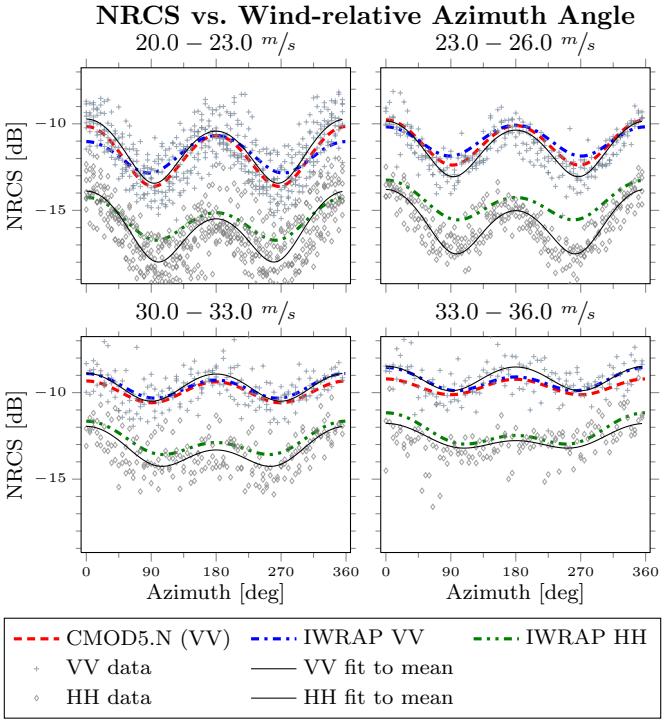

Fig. 4. NRCS at an incidence angle of 50° versus wind-relative azimuth angle grouped by wind speed. The model functions shown are computed with the mean wind speed observed in each wind speed range. Mean NRCS samples at each incidence angle from each circle are shown as gray plus symbols (VV-pol) and gray diamond symbols (HH-pol). A function in the form of $A + B\cos\,\chi + C\cos\,2\chi$ is fitted to the mean of each polarization's samples within a wind speed group and is shown as a solid line. The coefficients for each fit are reported in Table III and Table IV. CMOD5.N is shown as a dashed line and the IWRAP GMFs are shown as dash-dotted lines.

TABLE V
COEFFICIENTS FOR THE FIT OF THE MEAN POLARIZATION RATIO AS A FUNCTION OF WIND-RELATIVE AZIMUTH ANGLE TO $A + B\cos\,\chi + C\cos\,2\chi$ IN LINEAR UNITS

Wind Speed Group ($\mathrm{m\,s^{-1}}$)	A	B	C
20.0–23.0	1.9661	$-1.6399 \cdot 10^{-1}$	$4.0108 \cdot 10^{-2}$
23.0–26.0	1.9162	$-1.3179 \cdot 10^{-1}$	$-3.5722 \cdot 10^{-2}$
30.0–33.0	1.7628	$-1.6599 \cdot 10^{-1}$	$1.399 \cdot 10^{-2}$
33.0–36.0	1.7406	$-7.9928 \cdot 10^{-2}$	$5.8588 \cdot 10^{-2}$

Fig. 5 shows the polarization ratio as a function of wind-relative azimuth angle at 50° incidence. The data points from each circle flight are shown as gray circles. The function $A + B\cos\,\chi + C\cos\,2\chi$ is fitted to the mean and is shown as a solid line; the coefficients for each fit are reported in Table V. For reference, the polarization ratio from [3] at 50° incidence is shown as a horizontal dashed line. There is a small but measurable wind-directional signature in the

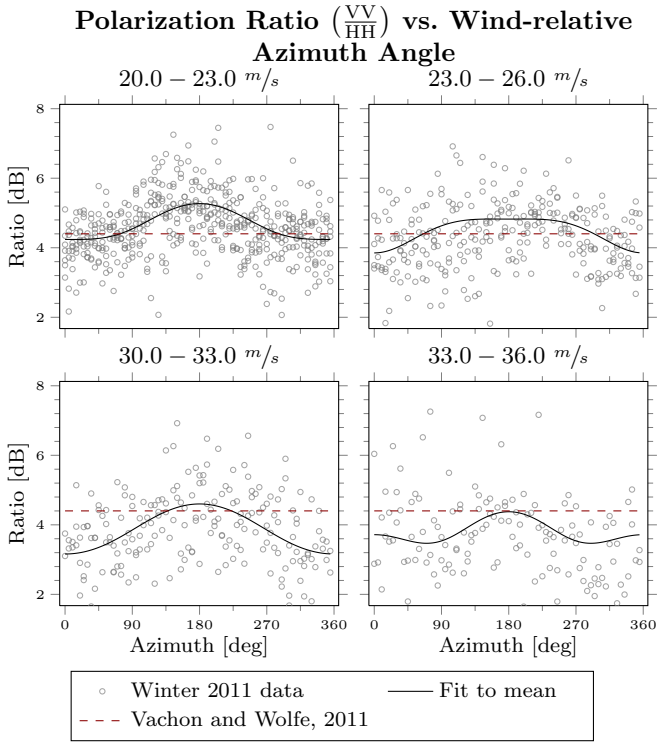

Fig. 5. Polarization ratios VV/HH at incidence angle 50° versus wind-relative azimuth angle grouped by wind speed. Ratios of the mean NRCS sampled from each circle flight between 48° and 52° incidence are averaged in 5° azimuth bins and are shown as gray open circles. A function in the form of $A + B\cos\ \chi + C\cos\ 2\chi$ is fitted to the mean and is shown as a solid line. The coefficients for each fit are reported in Table V. The polarization ratio from [3] at 50° is shown for reference as a horizontal dashed line.

polarization ratio data from the Winter 2011 experiment. This is consistent with earlier observations [4], [6], [12]. There was no analytical relationship for polarization ratio as a function of azimuth angle proposed in [4]. Moreover, while an analytical relationship with azimuth angle dependence was proposed in [12], it is only valid between 10° and 43° incidence. As a result, we only verify the observations in [4], [12] that the polarization ratio appears to have a maximum in the downwind direction for the wind speeds and incidence angles sampled.

V. Summary

We have reported observations of the dual-polarized sea surface NRCS at C-band under high winds ($20\,\mathrm{m\,s^{-1}}$ to $36\,\mathrm{m\,s^{-1}}$) over a range of incidence angles (32° to 60°). We find that the polarization ratio behavior at lower wind speeds is well described by the expression in [3], even when extrapolating beyond their measurements. However, in all wind speed groups, we observe that the slope of the polarization ratio in decibels appears to change more drastically than indicated by recent models. We also observe dependence of polarization ratio on wind speed; as wind speed increases, the slope of the polarization ratio in decibels as a function of incidence angle decreases. Finally, we observe a small but measurable wind-directional signature in the polarization ratio, which is consistent with earlier observations [4], [6], [12].

Acknowledgment

The authors gratefully acknowledge the crew of N43RF and the generous logistical and technical support of the NOAA Aircraft Operations Center in Tampa, FL. The authors also acknowledge the efforts of M. Baker (NOAA) and T. Hartley (UMass) in instrumentation support.

References

[1] F. M. Monaldo, D. R. Thompson, R. C. Beal, W. G. Pichel, and P. Clemente-Colon, "Comparison of SAR-derived wind speed with model predictions and ocean buoy measurements," *IEEE Trans. Geosci. Remote Sens.*, vol. 39, no. 12, pp. 2587–2600, Dec. 2001.

[2] P. W. Vachon and F. W. Dobson, "Wind retrieval from RADARSAT SAR images: selection of a C-band HH polarization wind retrieval model," *Can. J. Remote Sens.*, vol. 26, no. 4, 306–313, 2000.

[3] P. W. Vachon and J. Wolfe, "C-band cross-polarization wind speed retrieval," *IEEE Geosci. and Remote Sens. Lett.*, vol. 8, no. 3, pp. 456–459, May 2011. DOI: 10.1109/LGRS.2010.2085417.

[4] B. Zhang, W. Perrie, and Y. He, "Wind speed retrieval from RADARSAT-2 quad-polarization images using a new polarization ratio model," *J. Geophys. Res.*, vol. 116, Aug. 2011. DOI: 10 . 1029 / 2010JC006522.

[5] D. Fernandez, E. Kerr, A. Castells, J. Carswell, S. Frasier, P. Chang, P. Black, and F. Marks, "IWRAP: the imaging wind and rain airborne profiler for remote sensing of the ocean and the atmospheric boundary layer within tropical cyclones," *IEEE Trans. Geosci. and Remote Sens.*, vol. 43, no. 8, pp. 1775–1787, Aug. 2005. DOI: 10.1109/TGRS.2005.851640.

[6] D. E. Fernandez, J. R. Carswell, S. Frasier, P. S. Chang, P. G. Black, and F. D. Marks, "Dual-polarized C- and Ku-band ocean backscatter response to hurricane-force winds," *J. Geophys. Res.*, vol. 111, no. C8, 2006. DOI: 10.1029/2005JC003048.

[7] E. W. Uhlhorn and P. G. Black, "Verification of remotely sensed sea surface winds in hurricanes," *J. Atmos. Ocean. Technol.*, vol. 20, no. 1, pp. 99–116, Jan. 2003. DOI: 10.1175/1520-0426(2003)020⟨0099:VORSSS⟩2.0.CO;2.

[8] R. J. Doviak and D. S. Zrnić, *Doppler Radar and Weather Observations: Second Edition*. Dover Publications, May 2006.

[9] W.-C. Lee, P. Dodge, F. D. J. Marks, and P. H. Hildebrand, "Mapping of airborne doppler radar data," *J. Atmos. Ocean. Technol.*, vol. 11, no. 2, pp. 572–578, Apr. 1994.

[10] H. Hersbach, A. Stoffelen, and S. de Haan, "An improved C-band scatterometer ocean geophysical model function: CMOD5," *J. Geophys. Res.*, vol. 112, no. C3, Mar. 2007. DOI: 10.1029/2006JC003743.

[11] D. Thompson, T. Elfouhaily, and B. Chapron, "Polarization ratio for microwave backscattering from the ocean surface at low to moderate incidence angles," in *Proc. 1998 IEEE Int. Geosci. and Remote Sens. Symp.*, vol. 3, Seattle, WA, USA: IEEE, 1998, pp. 1671–1673. DOI: 10.1109/IGARSS.1998.692411.

[12] A. Mouche, D. Hauser, J.-F. Daloze, and C. Guerin, "Dual-polarization measurements at C-band over the ocean: results from airborne radar observations and comparison with ENVISAT ASAR data," *IEEE Trans. Geosci. and Remote Sens.*, vol. 43, no. 4, pp. 753–769, Apr. 2005. DOI: 10.1109/TGRS.2005.843951.